

Twist, turn and encounter: the trajectories of small atmospheric particles unravelled

Taraprasad Bhowmick^{1,2}, Yong Wang¹, Jonas Latt³ and Gholamhossein Bagheri¹

Corresponding authors: Gholamhossein Bagheri, gholamhossein.bagheri@ds.mpg.de; Yong Wang, yong.wang@ds.mpg.de

(Received 10 February 2025; revised 16 July 2025; accepted 31 August 2025)

Solid atmospheric particles, such as ice crystals, pollen, dust, ash and microplastics, strongly influence Earth's climate, ecosystems and air quality. Previous studies have typically relied on analytical models valid only for very small particles or experiments in liquids, where the particle-to-fluid density ratio R is much lower than values encountered in the atmosphere. We combine a novel experimental set-up with particle-resolved direct numerical simulations to study the settling of sub-millimetre ellipsoids in still air. Particle shapes span elongation and flatness values $0.2 \le EL$, $FL \le 1.0$ at a density ratio R =1000 and particle Reynolds numbers $2.1 < Re_p < 4.5$, a regime well below the onset of wake-induced instabilities. Nonetheless, we observe unexpectedly rich dynamics: all non-spherical particles exhibit damped oscillatory motion, and some triaxial ellipsoids follow fully three-dimensional, non-planar trajectories due to rotation about all three axes. Simulations at lower density ratios (R = 10, 100) confirm that these behaviours are driven by strong lateral forces happening only at R = 1000. Key settling characteristics exhibit nonlinear and non-trivial dependencies on shape. In the two-dimensional phase space of elongation and flatness, settling velocity is symmetric about the principal diagonal (EL = FL), while oscillation frequency and damping rate show symmetry about the antidiagonal. Flatness strongly influences pressure drag, while elongation governs lateral drift and swept volume, which can reach up to ten times the particle diameter and four times the volume-equivalent sphere, respectively.

Key words: atmospheric flows, particle/fluid flows

¹Max Planck Institute for Dynamics and Self-Organization, Am Faßberg 17, Göttingen D-37077, Germany

²University of Göttingen, Friedrich-Hund-Platz 1, Göttingen D-37077, Germany

³University of Geneva, 24 rue du Général-Dufour, Genève CH-1211, Switzerland

1. Introduction

There are numerous examples of non-spherical atmospheric particles from both natural and anthropogenic sources. Examples include volcanic (Rossi et al. 2021) and wildfire (Bodí et al. 2014) ashes, sand (Merrison 2012), dust (Mahowald et al. 2014; van der Does et al. 2018) and microplastics (Brahney et al. 2020; Tatsii et al. 2023; Reininger et al. 2025) (see figure 1a). Those particles are known to have various impacts, from increasing health risks for humans (Horwell & Baxter 2006; Manisalidis et al. 2020; Zhang et al. 2020a) to the radiative properties of clouds (Baran 2012; Matus & L'Ecuyer 2017), which influence the weather and climate (Ramanathan et al. 1989; Norris et al. 2016). However, our understanding of the transport properties of these particles is rather limited. This is due to the lack of theoretical models for heavy particles larger than 0.1 mm in air, and the existing experimental data come almost exclusively from studies conducted in liquids. The experiments in liquids (e.g. Willmarth, Hawk & Harvey 1964; Jayaweera & Cottis 1969; Field et al. 1997; Belmonte, Eisenberg & Moses 1998; Lopez & Guazzelli 2017; Roy et al. 2019, 2023; Esteban, Shrimpton & Ganapathisubramani 2020; Will et al. 2021; Baker & Coletti 2022; Cabrera et al. 2022; Giurgiu et al. 2024), in which the dynamic similarity is observed using the particle Reynolds number Re_p , provide many insightful findings on the settling behaviour of non-spherical particles, with

$$Re_p = \frac{D_{eq}v_T}{v},\tag{1.1}$$

where D_{eq} is the diameter of a volume-equivalent sphere, v_T is the terminal velocity of the particle, and v is the kinematic viscosity of the ambient fluid. Here, Re_p quantifies the relative importance of the inertial forces compared to the viscous forces acting on the particle (Happel & Brenner 1983; Khayat & Cox 1989; Gustavsson *et al.* 2019).

However, the ratio of particle to fluid density

$$R = \frac{\rho_p}{\rho_f},\tag{1.2}$$

which in air is typically of the order of 1000 for most solid particles, cannot exceed much beyond 10 in liquids, as summarised in figure 1(b). Recent experiments at low Reynolds numbers in air, particularly for axisymmetric shapes such as spheroids, have advanced our understanding considerably. Analytical and empirical approaches reveal that particle inertia strongly affects settling dynamics, often inducing pronounced transient oscillations (Bhowmick *et al.* 2024) or sustained orientation instabilities at Reynolds numbers much lower than those observed at low R (Tinklenberg, Guala & Coletti 2023). While these findings clarify the behaviour of axisymmetric particles or thin disks, the broader phase space remains unexplored, in particular regarding how non-axisymmetric features shape settling at Reynolds numbers applicable to a wide range of atmospheric particles, i.e. $1 < Re_p < 10$ at R = 1000 as shown in figure 1(b). This raises a critical question: how do these non-axisymmetric features, which are key to generalising our insights across the diverse shapes in the atmosphere, affect settling dynamics?

This study targets the parameter range $1 < Re_p < 10$ at R = 1000 ($\rho_p = 1200$ kg m⁻³ and $\rho_f = 1.2$ kg m⁻³), which is relevant for many atmospheric particle sources yet remains largely unexplored experimentally or numerically. We examine the settling of heavy ellipsoids of various shapes in still air, leveraging their utility as surrogates for irregular particles (Bagheri & Bonadonna 2016). By combining novel experiments with particle-resolved direct numerical simulations (DNS), we uncover complex transient dynamics and

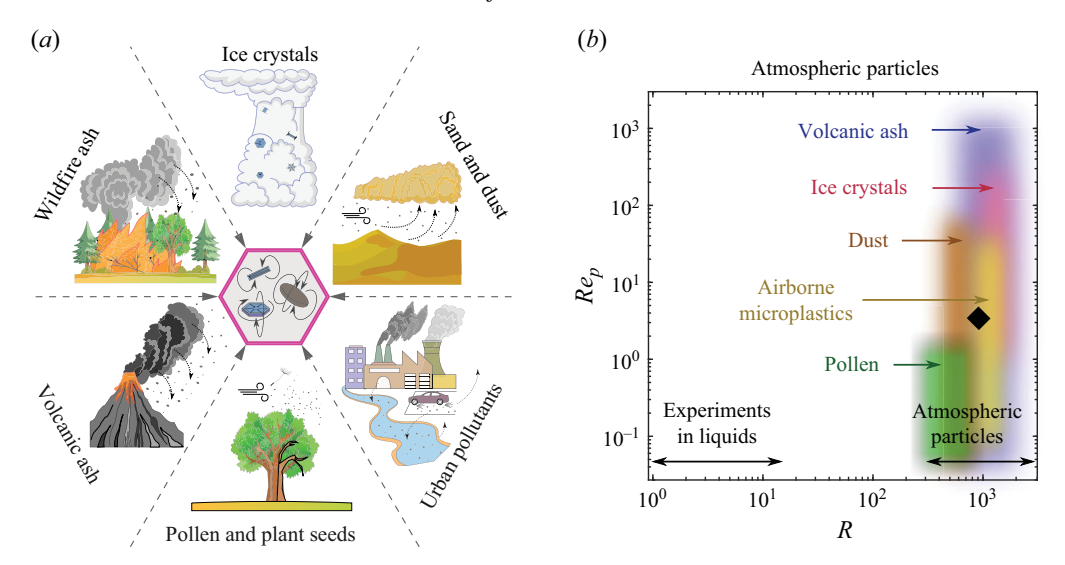


Figure 1. (a) Natural and anthropogenic sources of non-spherical solid particles that impact the weather, climate and ecosystems. (b) Atmospheric particles in the phase space of particle Reynolds number Re_p and particle to fluid density ratio R (Kajikawa 1972, 1992; van Hout & Katz 2004; Pruppacher & Klett 2010; Bagheri & Bonadonna 2016; Allen *et al.* 2019; Zhang *et al.* 2020b). The relevant Re_p and R of this current study are shown with the black \diamond .

highlight a largely uncharted regime of non-spherical particle behaviour, with important implications for understanding particle-rich atmospheric environments.

2. Methods

2.1. Experiments

The Göttingen Turret, the experimental set-up for this study, is developed at the Max Planck Institute for Dynamics and Self-Organization (MPI-DS). It features four synchronised high-speed cameras – TX, TY, BX and BY – imaging an air-filled glass chamber (GC) where particles are injected by a particle injector (PI) and fall under gravity in still air, as shown in figure 2(a,b). Two cameras capture each of two overlapping volumes from orthogonal directions (see figure 2b), enabling full three-dimensional (3-D) tracking of particles with at least one dimension $\geq 100 \,\mu\text{m}$.

All cameras are equipped with Nikon ED AF Micro Nikkor 200 mm lenses, operated at F-stop 22 and 1:1 magnification, resulting in an image pixel size of 6.75 μ m px⁻¹. The effective exposure time is 2.5 μ s. The camera system is synchronised in a leader-follower configuration, with camera TX acting as the leader, and its strobe signal used to synchronise the remaining three follower cameras. Given the fixed data throughput of 9 Gpx s⁻¹ (Phantom VEO-Series, Vision Research, AMETEK), maximising spatial resolution required a trade-off with temporal resolution. We employed the maximum available resolution 4096 px in the Z (falling) direction, corresponding to a vertical observation window of approximately 28 mm per camera at 1:1 magnification, yielding a total vertical measurement distance of approximately 55 mm when the top and bottom camera fields of view are combined. The horizontal field of view is 720 px (4.86 mm). Images are captured at frame rate 2932 frames per second. At this temporal resolution, changes in the angular motion of the particles are sufficiently small to allow for accurate

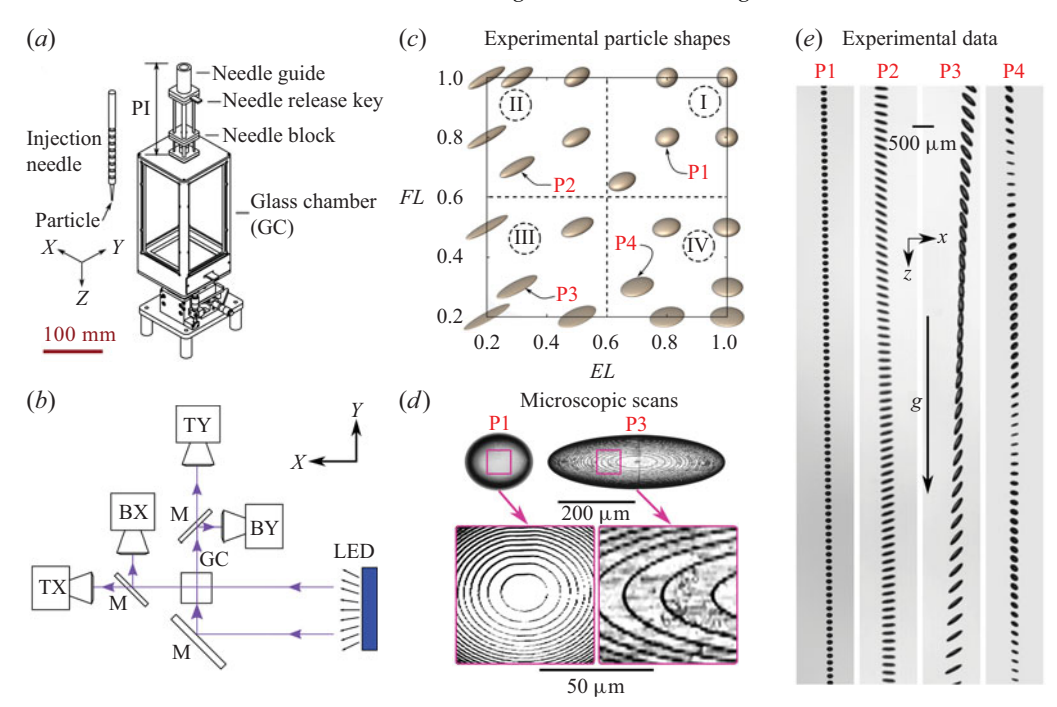


Figure 2. (a) A 3-D CAD drawing of the air-filled glass chamber (GC) and the particle injector (PI) for releasing particles inside the GC. (b) Schematic representation of the illumination of the GC and the positioning of the mirrors (M) for imaging the particles by the upper TX and TY cameras, and the lower BX and BY cameras. Axis Z is in the direction of gravity. (c) The shapes of ellipsoidal, non-spherical particles of this study are defined with two shape parameters – elongation EL and flatness FL – keeping the volume constant (equivalent to a sphere of 140 μ m diameter D_{eq}). The particle shape-space is divided into four categories: I – near spherical, II – prolate/elongated, III – highly non-spherical ellipsoidal, and IV – oblate/flattened shapes. (d) Laser microscope scans of two 3-D printed particles from categories I and III. The 3-D surface features are <1 μ m in size. (e) Experimental observation of oscillations in angular orientation and lateral drift when non-spherical particles are falling under gravity g. Images (a) and (b) are adjusted from figure S1 in the supplementary information of Bhowmick et al. (2024).

reconstruction of angular dynamics, typically below 100 Hz. A detailed description of the set-up is provided in Bhowmick *et al.* (2024).

Ellipsoids are 3-D-printed using a NanoScribe system (Photonic Professional (GT) User Manual, Nanoscribe GmbH 2015), achieving surface resolution $\leq 0.3 \,\mu m$. The photoresist acrylic resin IP-S (CH_{1.72}N_{0.086}O_{0.37}) is polymerised via two-photon polymerisation (Liu *et al.* 2018). The particles are printed in stacked polymerised layers $\leq 0.6 \,\mu m$ thick, with mass density $\rho_p = 1200 \,\mathrm{kg} \,\mathrm{m}^{-3}$, matching many atmospheric particles (see figure 1b).

For imaging, particles are carefully transferred from the glass substrate to an injection needle for controlled release into the air-filled glass chamber, which is positioned in such a way that the cameras capture the transient settling motion of particles a few centimetres (adjustable) below the detachment point of the injection needle. All particles are initially placed on the tip of the injection needle so that their largest surface area is in contact with the needle. Such an arrangement results in their maximum projected area being oriented normal to gravity. However, high-speed imaging of the release process (performed in separate experiments) revealed that the initial orientation cannot be reliably controlled. In some instances, particles detach in arbitrary orientations with non-zero lateral velocity, despite consistent placement. The initial release vertical velocity, however, can be controlled to some extent by adjusting the vertical position from which the needle

is released (Bhowmick *et al.* 2024). This height was adjusted such that for the majority of core experiments for a given shape, both the transient and terminal phases of the settling motion occurred entirely within the tracking volume.

The vertical distance between the detachment point of the particle from the injection needle and the start of the imaging field is adjustable and is selected to ensure that both transient dynamics and the terminal settling state are fully captured. The terminal state is defined as the point in time at which the vertical acceleration of the particle $|a_z|$ falls below $0.2 \,\mathrm{m \, s^{-2}}$. This threshold was chosen based on an analysis of vertical acceleration profiles within the field of view, and serves as a conservative lower bound that accounts for all measurement uncertainties. We also calculated particle lateral drift δ , which is defined as the total lateral path length traversed by the particle (normal to gravity) in the xy-plane over fixed settling distance 55 mm (corresponding to the full height of the combined observation volume). As mentioned above, there may be non-zero initial lateral velocities when particles are injected; however, these do not constitute systematic biases. Therefore, we focus on the general statistical analysis of lateral drifts based on the experimental measurements. Further details on the 3-D calibration procedure, sub-pixel spatial accuracy, and computation of velocity and acceleration can be found in Bhowmick *et al.* (2024).

The particles of this study are of ellipsoidal shape, defined by two shape parameters: elongation EL, and flatness FL, as visualised in figure 2(c) and defined as

$$EL = \frac{I}{L}, \quad FL = \frac{S}{I}, \tag{2.1}$$

where L, I and S are the longest, intermediate and shortest dimensions of the particle, which are orthogonal to each other. The main characteristics of the ellipsoids investigated here are summarised in table 1. The shapes considered in this study are divided into four categories, each containing an equal number of cases. The particle shape space is categorised as follows: category I – near-spherical, II – prolate/elongated, III – highly non-spherical ellipsoidal, and IV – oblate/flattened shapes (figure 2c). The control parameter in our experiment is the particle mass (or volume), which is equal to that of a volume-equivalent sphere with diameter $D_{eq} = 140 \,\mu\text{m}$ for all particles. The particles are produced using two-photon polymerisation 3-D printing, which enables us to achieve an explicit control over particle shape and size with sub-micrometre printing resolution; e.g. see microscope images of the manufactured particles in figure 2(d).

Highernon-sphericity causes increased drift from the observation volume, affecting imaging success rates. The sphere had the highest success rate (34.4%), while the ellipsoid with most flatness and elongation (EL = FL = 0.2) had the lowest (11.5%). Data analysis follows a camera model (Tsai 1987) to generate 3-D world coordinates from calibration grid images. The centre of mass and longest particle length are determined via ellipsoid fitting, and the velocity and angular orientation are extracted accordingly (Bhowmick *et al.* 2024).

2.2. Simulations

We employed particle-resolved DNS based on the lattice Boltzmann method (LBM) (Succi 2001) to model the settling dynamics of atmospheric particles in a quiescent fluid. The numerical solver Palabos Turret (Bhowmick *et al.* 2025*a,b*), originally developed by the Palabos group (Latt *et al.* 2021) at the University of Geneva, was further modified and verified at the MPI-DS for this study. It solves the quasi-incompressible Navier–Stokes equations via the LBM and Newton's equations for particle motion, coupled through the immersed boundary method (IBM) (Ota, Suzuki & Inamuro 2012). It is validated through comparisons with analytical predictions and experimental observations of the free-fall

Category no.	EL	FL	$L (\mu m)$	$I (\mu m)$	$S(\mu m)$	Re_p	$\tau_p \text{ (ms)}$	Exp/DNS
I	1.00	1.00	140.0	140.0	140.0	4.49	71.77	$\sqrt{}$
I	0.80	0.80	175.0	140.0	112.0	4.31	89.72	
I	0.65	0.65	215.4	140.0	91.0	4.03	110.43	×✓
I	1.00	0.80	150.8	150.8	120.6	4.40	83.27	$\sqrt{\checkmark}$
I	0.80	1.00	162.0	130.0	130.0	4.47	77.12	$\sqrt{}$
II	0.50	1.00	222.2	111.0	111.0	4.19	90.32	$\sqrt{}$
II	0.30	1.00	312.4	93.7	93.7	3.78	107.21	×√
II	0.20	1.00	410.0	81.8	81.8	3.36	122.81	$\sqrt{\checkmark}$
II	0.50	0.80	239.4	119.7	95.8	4.02	104.94	$\sqrt{\checkmark}$
II	0.20	0.80	441.0	88.0	70.6	3.21	142.11	
II	0.30	0.70	352.0	106.0	74.0	3.49	136.63	$\sqrt{\checkmark}$
III	0.50	0.50	280.0	140.0	70.0	3.60	143.55	$\sqrt{\checkmark}$
III	0.30	0.30	466.0	140.0	42.0	2.76	238.90	$\sqrt{\checkmark}$
III	0.20	0.20	700.0	140.0	28.0	2.13	358.86	$\sqrt{\times}$
III	0.50	0.20	380.0	190.0	38.0	2.78	264.39	$\sqrt{\ }$
III	0.20	0.50	515.8	103.1	51.6	2.81	194.73	$\sqrt{\checkmark}$
IV	1.00	0.50	176.4	176.4	88.2	3.99	113.95	$\sqrt{\checkmark}$
IV	1.00	0.30	209.1	209.1	62.7	3.55	160.11	$\times $
IV	1.00	0.20	239.4	239.4	47.9	3.15	209.87	$\sqrt{\ }$
IV	0.80	0.50	204.7	163.7	81.9	3.89	122.71	$\sqrt{\ }$
IV	0.80	0.20	277.8	222.2	44.4	3.06	226.04	$\sqrt{\ }$
IV	0.70	0.30	266.0	186.0	56.0	3.38	181.17	$\sqrt{\checkmark}$

Table 1. Details of the particles, with category numbers, shape parameters elongation EL and flatness FL. Here, $Re_p = D_{eq} v_T / v$ is the particle Reynolds number based on the equivalent sphere diameter $D_{eq} = 140 \,\mu\text{m}$ and on the observed terminal velocity v_T from the DNS. The Stokes time $\tau_p = (\rho_p / 18 \rho_f) LI / v$ provides an estimate of the particle response time, where $\rho_p = 1200 \, \text{kg m}^{-3}$ and $\rho_f = 1.2 \, \text{kg m}^{-3}$ are the mass-densities of the particle and the air, respectively, and $v = 1.5 \times 10^{-5} \, \text{m}^2 \, \text{s}^{-1}$ is the kinematic viscosity of air. For all the particles shown in this table, R = 1000. A $\sqrt{}$ indicates the presence of data; otherwise, a \times is shown.

dynamics of particles of different shapes, including spheres, ellipsoids and volcanic fragments, across a wide range of Re_p (Bhowmick *et al.* 2025*a*).

Palabos Turret utilises a regularised LBM with a BGK collision operator (Bhatnagar, Gross & Krook 1954) to resolve the 3-D flow field with a uniform Eulerian mesh. The fluid is modelled as particle populations, which follow the evolution rule as

$$f_i(\mathbf{x} + \mathbf{\xi}_i \,\delta t, t + \delta t) = f_i^{(0)} + \left(1 - \frac{1}{\tau}\right) f_i^{(1)}.$$
 (2.2)

Here f_i , $f_i^{(0)}$ and $f_i^{(1)}$ are the particle distribution function and its equilibrium and off-equilibrium populations, respectively (Bhowmick *et al.* 2025*a*). The index $i=0,\ldots,q-1$ identifies the elements of a discretised velocity space $\{\boldsymbol{\xi}_i\}_{i=0}^{q-1}$, which is represented by the D3Q27 lattice; $\delta \boldsymbol{x}$ and δt are the spatial and temporal resolutions, respectively; and τ is the relaxation time, which relates to the kinematic viscosity ν through the speed of sound c_s as

$$v = c_s^2 \, \delta t \left(\tau - \frac{1}{2} \right). \tag{2.3}$$

Macroscopic variables of the fluid, such as density ρ and velocity u, can be calculated by taking a weighted sum of the particle populations:

$$\rho = \sum_{i} f_i, \quad \mathbf{u} = \frac{\sum_{i} \xi_i f_i}{\sum_{i} f_i}.$$
 (2.4)

The hydrodynamic stress tensor σ , which is used for the evaluation of the fluid forces on the solid surface, can be obtained directly from f_i as

$$\boldsymbol{\sigma} = -p\boldsymbol{I} + \left(\frac{1}{2\tau} - 1\right) \sum_{i} \boldsymbol{\xi}_{i} \boldsymbol{\xi}_{i} \left(f_{i} - f_{i}^{0}\right). \tag{2.5}$$

Here, $p = c_s^2 \rho$ is the fluid pressure, and I is the identity matrix. The first (second) term on the right-hand side of (2.5) corresponds to the pressure (friction) component of the stress tensor.

Solid particles, represented by non-deformable Lagrangian surface meshes, are immersed in the fluid and allowed to move and rotate freely (figure 3). Given a total force F acting on a particle of mass m, the position of its centre of mass x, translational velocity v and angular velocity ω are governed by

$$\frac{\mathrm{d}x}{\mathrm{d}t} = \mathbf{v}, \quad \frac{\mathrm{d}\mathbf{v}}{\mathrm{d}t} = \frac{\mathbf{F}}{m}, \quad \frac{\mathrm{d}\mathbf{d}}{\mathrm{d}t} = \boldsymbol{\omega},$$
 (2.6)

respectively. Here, d is an orthonormal triad attached to the particle and following its motion. With inertia tensor J and torque T, the evolution of the particle's rotation is

$$\frac{\mathrm{d}}{\mathrm{d}t}\boldsymbol{\omega} = \boldsymbol{J}^{-1}\boldsymbol{T}.\tag{2.7}$$

Forces on the particles, such as gravity and fluid-induced inertia, are computed using the IBM. In particular, the 'multi-direct forcing' approach (Ota *et al.* 2012), with an iterative procedure, is used to couple translational and rotational dynamics between fluid and particle.

Similar to the experimental set-up, the computational domain is a rectangular chamber with constant pressure (i.e. density) imposed at the top, a no-slip condition at the bottom, and periodic boundaries on the lateral sides, as shown in figure 3(a). Based on mesh independence tests carried out on various shapes, we have found that the lateral width of the computational domain must be at least 10 times the largest particle dimension, L, to minimise the wall effects. It is also found that at least 10 fluid points in the smallest particle dimension are needed to resolve the boundary layers, and to ensure reliable simulations of translational and rotational dynamics (figure 3b). The spatial resolutions of the fluid and solid surface meshes are approximately matched, with resolution ratio close to unity (figure 3c). These constraints make it computationally infeasible to simulate the full settling trajectory, from rest to terminal velocity, within a single domain. For a computational domain of size $10L \times 10L \times 1000L$, with mesh resolution $\Delta x = S/10$, the total number of mesh points becomes $(10L/\Delta x)^2 \times (1000L/\Delta x) = 10^8 L^3/S^3$. For a typical case with EL = I/L = 0.3 and EL = S/I = 0.3, this gives $EL = EL \times EL = 0.09$, thus the total number of mesh points is approximately EL = I/L = 0.3 and EL = I/

To address the computational challenges of simulating particle settling over long distances, we developed a truncated settling chamber, illustrated in figure 3(a), which is comprehensively discussed and validated in Bhowmick *et al.* (2025a). The domain vertically spans approximately three times the lateral width, amounting to approximately 30L for the particles considered in this study, and is divided into three vertical sections: (i) a sponge zone at the top, occupying 10% of the total height, designed to damp spurious pressure waves generated by numerical artefacts; (ii) a central region where the particle

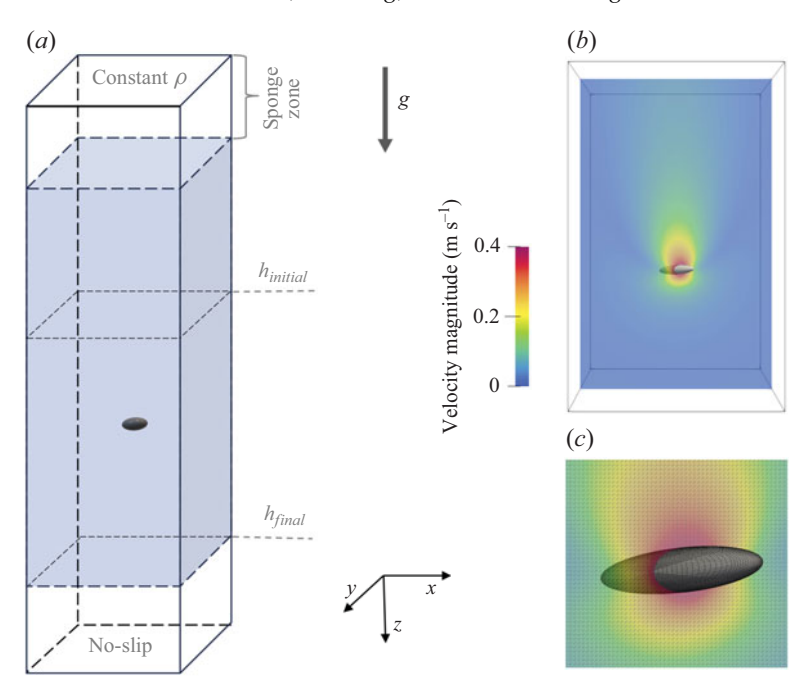


Figure 3. (a) The 3-D computational domain showing a particle (black ellipsoid) at an intermediate stage of settling under gravity in the z-direction, after being released from rest at height $h_{initial}$. Periodic boundary conditions are applied laterally, while the top boundary is held at constant pressure, and the bottom boundary is a no-slip (wall) boundary. (b) An exemplary simulated particle with EF = 0.2 and FL = 1.0, shown alongside a portion of the surrounding fluid domain. The cross-sectional colour map represents the local velocity field. (c) A close-up view of (b), showing the uniform Eulerian mesh in the fluid domain, and the Lagrangian surface mesh on the particle.

settles sufficiently at distance from all domain boundaries; and (iii) a near-ground zone at the bottom, also comprising 10 % of the total height. The bottom boundary, representing a no-slip wall, serves to prevent artificial air entrainment and downward flow that could arise if periodic boundary conditions were used on both the top and bottom boundaries.

The particles simulated in this study are released with initial velocity zero and oriented such that the longest dimension, L, is aligned with gravity, resulting in the minimum projection area perpendicular to gravity at the initial release height $h_{initial}$ (figure 3a). Once the particle reaches a lower height h_{final} , both the particle and the surrounding flow field are duplicated and repositioned at the top of the computational domain, effectively resetting the particle to its initial height $h_{initial}$ to continue its descent. This copy-and-reposition procedure is repeated until the particle reaches its terminal state, defined as the point at which the vertical acceleration satisfies $|a_z| < 0.01 \,\mathrm{m \, s^{-2}}$. This approach enabled efficient simulation of various particle configurations without requiring a domain long enough to capture the entire settling trajectory. Nonetheless, the simulations remained computationally intensive. For instance, the most demanding case, with EL = FL = 0.3, was performed on the supercomputer Cobra at the Max Planck Computing and Data Facility, employing grid resolution $4.2 \,\mu \,\mathrm{m}$, a total of $4.11 \,\mathrm{billion}$ mesh nodes, and 15 360 MPI tasks, amounting to 3.1 million computing hours.

As mentioned earlier, Bhowmick *et al.* (2025*a*) have found very close agreement between numerical results obtained from Palabos Turret and experimental measurements for various regular and irregular shapes in a wide range of particle Reynolds numbers.

For the ellipsoids studied here, validations are also presented in § 3.1. The numerical simulations provided detailed information, including the particle's position, velocity, orientation and surface force distribution, and the surrounding velocity field. This comprehensive dataset from numerical simulations complements the experimental measurements and allows the two approaches to be cross-validated. Quantities measurable by both approaches for cross-validation include the terminal velocity, the lateral drift δ , and the oscillation frequency and decay rate of the oscillation amplitudes of the longest axis of the ellipsoid (L). In simulations, δ is defined as the total lateral path length traversed by the particle (normal to gravity) in the xy-plane until it reaches the terminal state. One-to-one comparison of δ between experiments and simulations is not possible since in experiments the initial conditions could not be controlled precisely enough (see § 2.1), although their statistical signatures can be compared. Additional quantities accessible only through simulations include the pressure and friction components of the drag force, as well as the total swept volumes in the lateral (Ψ_1) and vertical (Ψ_2) directions.

2.3. Normalisation

In the following, normalised parameters are denoted by *. The spatial coordinates x^* , y^* , z^* and the drift δ^* are normalised by the equivalent sphere diameter D_{eq} , and velocity v is normalised by the terminal settling speed v_T . Time t is normalised as $T^* = tv_T/D_{eq}$. The pressure components of the drag force on a particle are expressed in dimensionless form as $P^* = P/F_z$, where F_z denotes the vertical component of the drag force. The vertical and lateral swept volumes, Ψ_z^* and Ψ_\perp^* , are normalised by the particle volume $\pi D_{eq}^3/6$. In simulations, Ψ_\perp is defined as the total volume swept by the particle (normal to gravity) in the horizontal directions until it reaches the terminal state, whereas Ψ_z is the total volume swept by the particle in the vertical directions until it reaches the terminal state.

3. Results

3.1. Experimental observations

We have conducted a total of 262 successful experimental runs for different particle shapes and density ratio R=1000, with each shape having from 9 to 22 runs (see example snapshots from experiments in figure 2e). By covering a wide range of flattened and/or elongated ellipsoids, we comprehensively explore the phase space of diverse particle shapes. This approach also serves as an effective proxy for irregular particles with similar form (Bagheri & Bonadonna 2016), eliminating the need for infinite case-by-case investigations. The particle Reynolds number achieved here ranges from approximately $Re_p=2.1$ to 4.5, as also detailed in table 1. This is significantly lower than the threshold Reynolds number of approximately 100, beyond which an unstable falling pattern is observed due to hydrodynamic instabilities in the wake of the falling particles in air and in liquids (Willmarth *et al.* 1964; Ern *et al.* 2012; Auguste, Magnaudet & Fabre 2013; Esteban *et al.* 2020; Tinklenberg *et al.* 2023).

Our experiments show that ellipsoids of various shapes exhibit orientation oscillations and lateral drifts as they settle in still air at $2.1 \le Re_p \le 4.5$ and R = 1000. The more flattened (low FL) or elongated (low EL) the ellipsoids are, the more pronounced these effects become. The top view of the particle trajectories (figure 4a) and the histograms of lateral drift (figure 4b) show the intricate falling behaviour of the investigated particles observed in experiments. Across all shape categories, particularly in categories II–IV, there is a notable lateral drift exceeding $10D_{eq}$ during experiments. Some particles exhibit wavy

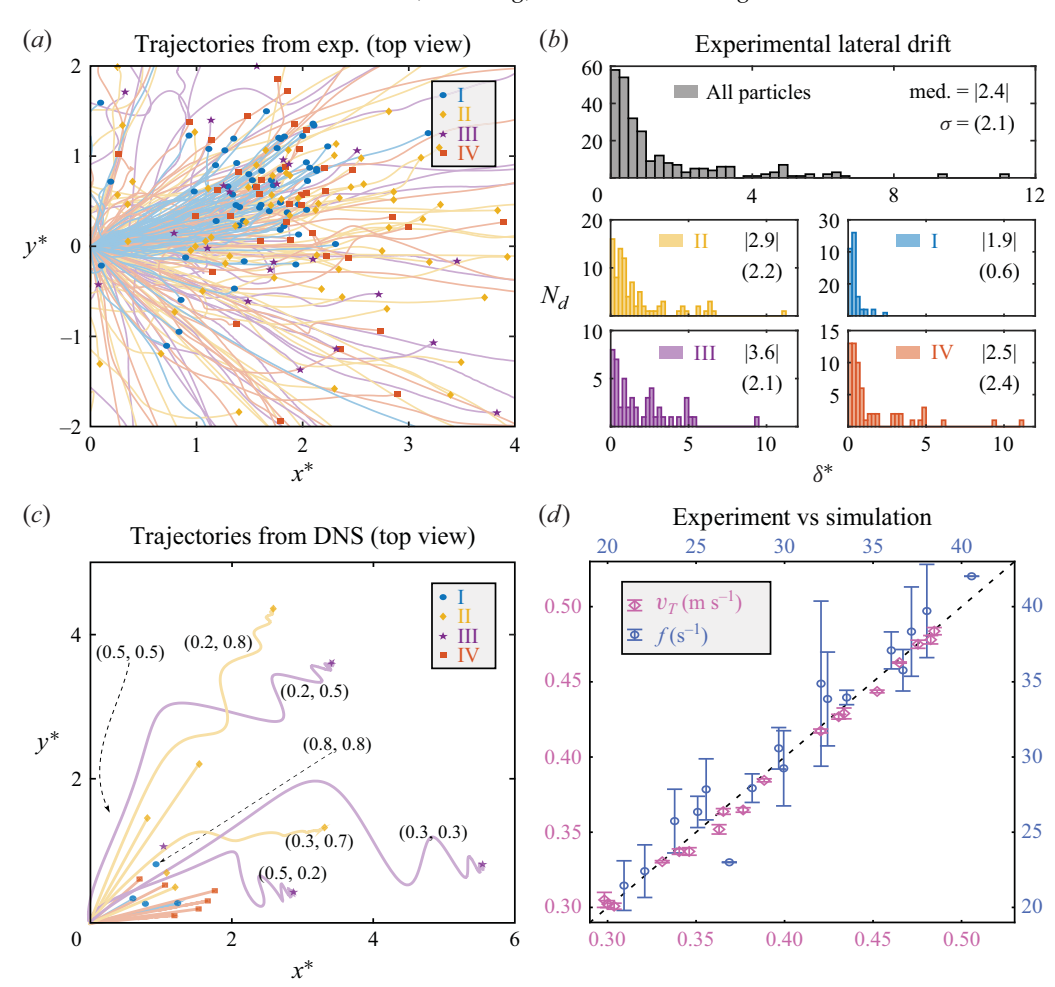


Figure 4. (a) Top view of the drifting trajectories of the non-spherical particles from experiments (zoomed in for better visibility) coloured by particle categories I–IV shown in figure 2(c). Here, x^* and y^* are the two lateral components normalised by D_{eq} . (b) Histograms of the normalised lateral drifts ($\delta^* = \delta/D_{eq}$) with bin width 0.25 δ^* from experimental measurements presented here. Here, δ is calculated as total lateral displacement in the xy-plane over fixed settling distance 55 mm, corresponding to the full height of the combined observation volume in experiments. Also, N_d is the number of experimental runs for a specific amount of δ^* , and the median and standard deviation values are shown as med. and σ . (c) Top view of the drifting particle trajectories from the DNS (rotated for better visibility), where the particles are released with zero initial velocity and minimum projection area normal to the falling direction. Shape parameters (EL, FL) for the non-planar trajectories are annotated next to the tracks. (d) Comparison of the terminal velocities v_T and frequencies of the angular oscillations f of the particles from experiments (vertical axes) and DNS (horizontal axes). The error bars are equivalent to one standard deviation variation. The dashed diagonal line shows 1:1 correspondence between experiments and DNS. The maxima of relative differences between the experiments and DNS are less than 3% and 10%, respectively, for v_T and f. We use R = 1000 for all the results presented in this figure.

lateral trajectories, while some others also make multiple sharp turns (figure 4a). The elongated particles in categories III and II have the highest median lateral drift, while the standard deviation of lateral drift in categories II–IV is four times higher than the near spherical particles in category I (figure 4b). As will be shown below, these lateral movements have a significant effect on the swept volume of the particles as they fall.

3.2. Numerical trajectories and validation

To fully understand the dynamics behind the complex trajectory of these particles at R=1000, we have replicated the experiments with large-scale DNS. As mentioned earlier, all simulations are carried out with a fixed initial condition, i.e. release with zero initial velocity and minimum projection area normal to the falling direction. Top views of DNS trajectories also reveal the wavy lateral motion of the particles (figure 4c), with sharp turns and lateral drifts up to $6D_{eq}$ for category III, compared to only one D_{eq} lateral drift for category I. Of the seven triaxial ellipsoids exhibiting non-planar motion, four belong to category III, two to category II, and one to category I, whereas none belongs to category IV. This suggests that non-planar motion is common in extremely flattened and elongated triaxial ellipsoids, but occurs more frequently in elongated particles than in flattened ones.

The excellent quantitative agreement between the experiments and DNS for the terminal velocity v_T and oscillation frequency f of the particles (figure 4d) suggests that many features of the transient dynamics are independent of initial conditions and could be generalised to real-world scenarios. For each shape, the standard deviation of v_T is less than 2% of its magnitude, and for f it is less than 16%, despite a large variability expected in the initial conditions of the experimental trajectories. This shows that the effects of the transient dynamics captured in the experiments are not dependent on initial conditions.

3.3. Effect of density ratio R

Having successfully validated our DNS against the experimental measurements, we turn our attention to distinguishing the role of particle to fluid density ratio R in the settling dynamics of non-spherical particles with the same Re_p . We have selected one particle shape (fixed EL and FL) from each of the particle categories I–IV, as shown in figure 5. The density ratios R considered in this subsection in addition to R = 1000 - i.e. R = 100 and 10 - are representative of typical conditions for volcanic ash/snow aggregates in the atmosphere and particles in water, respectively. As expected, particles need a longer settling distance before reaching terminal velocity as R increases. For instance, at R = 1000, the required $z^* = z/D_{eq}$ is approximately an order of magnitude longer than at R = 10 and 100.

A key new observation from figure 5 is that at R = 1000, the trajectories exhibit marked twists and turns, unlike at lower density ratios, for all the cases shown. The sequence of accelerating and decelerating intervals, as represented by the colours of the trajectories, also differs significantly at R = 1000, especially when compared to trajectories with R = 10. Similar to figure 4(c), different particle shapes/categories show clear influence on the lateral drift of the 3-D trajectories in figure 5. Near spherical ellipsoids (EL = FL = 0.8 of category I in figure 5b) show less lateral drift than the other categories. Spheroids (EL = 0.2, FL = 1.0 of category II in figure 5(a), and EL = 1.0, FL = 0.2 of category IV in figure 5(d)) exhibit lateral drift in a planar two-dimensional motion with amplitudes larger than the ellipsoid with EL = FL = 0.8. For the most non-spherical ellipsoid simulated here with EL = FL = 0.3, which is a category III shape in figure 5(c), significant lateral drifts up to five times D_{eq} combined with a complex 3-D motion are observed.

We further compare the key particle quantities from the DNS of the EL = FL = 0.3 ellipsoids at R = 1000, 100 and 10, but at the same $Re_p = 3$ in figure 6. As observed in figure 5(c), particles need a longer settling distance before reaching terminal velocity as R increases – for instance, at R = 1000, the required $z^* = z/D_{eq}$ is approximately 6.3 (3.6) times longer than at R = 10 (R = 100), which is an expected behaviour. However, during the transition to terminal state, orientation oscillations and force histories deviate

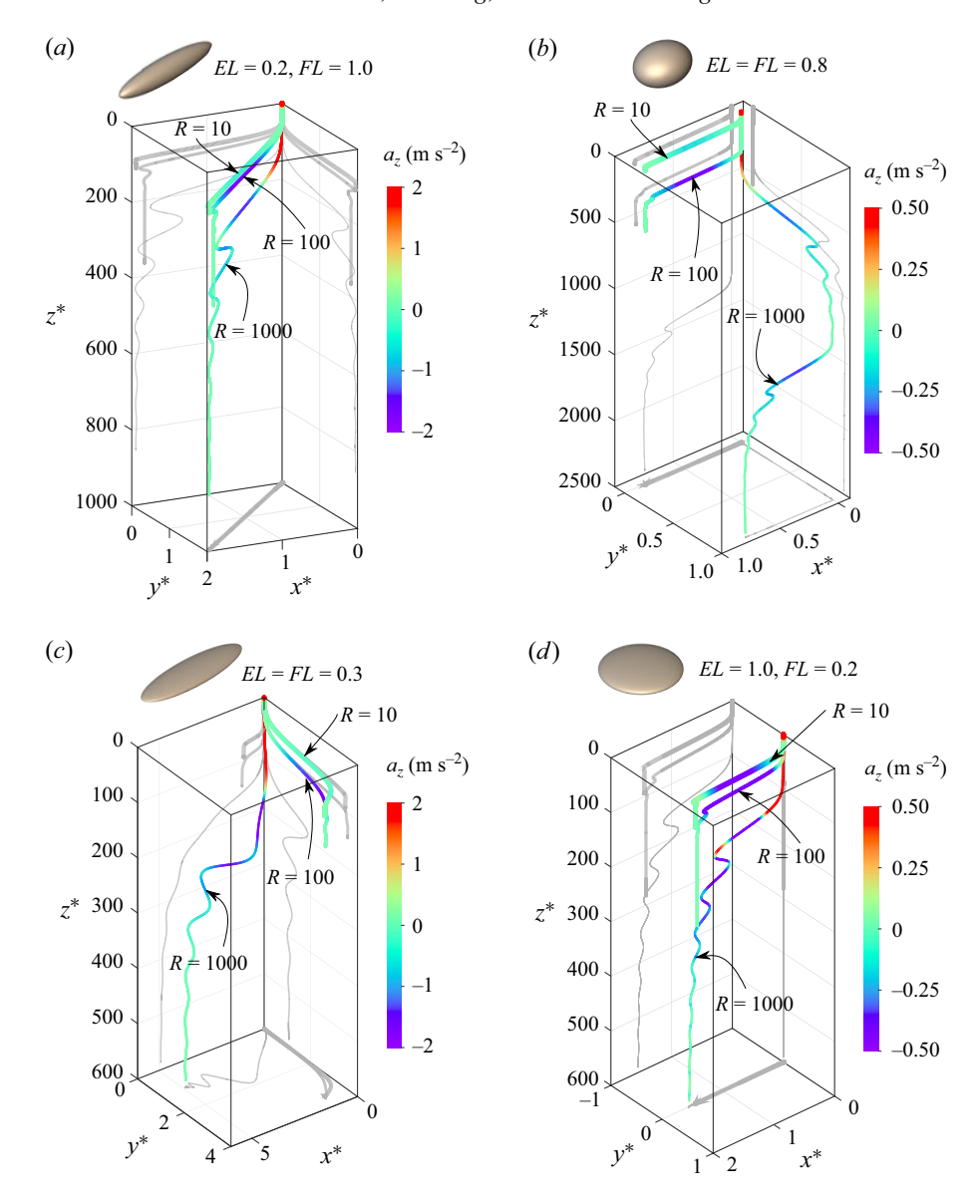


Figure 5. Settling dynamics of particles with four different shapes, each examined at density ratios R=1000, 100 and 10. The particle Reynolds number Re_p is held constant within each shape category. Trajectories of particles for (a) EL=0.2, FL=1.0 (category II), (b) EL=FL=0.8 (category I), (c) EL=FL=0.3 (category III), (d) EL=1.0, FL=0.2 (category IV). The 3-D trajectories are coloured by the instantaneous acceleration a_z , and their two-dimensional projections are coloured grey. Distances are normalised by D_{eq} .

significantly at R=1000 compared with R=10 or 100 (see figure 6). For example, oscillations and the progression of the transient motion to the final state also differ significantly for vertical v_T and lateral v_\perp velocity components as shown in figure 6(a,b), especially the latter showing strong fluctuations at R=1000. Figure 6(c,d) show that the damping of the amplitudes of the angular oscillations for the pitch angle φ_L (L-axis angle from horizon) and roll angle φ_L (L-axis angle from horizon) weakens as the density ratio R increases, leading to change from rapidly damped to under-damped oscillations. Another

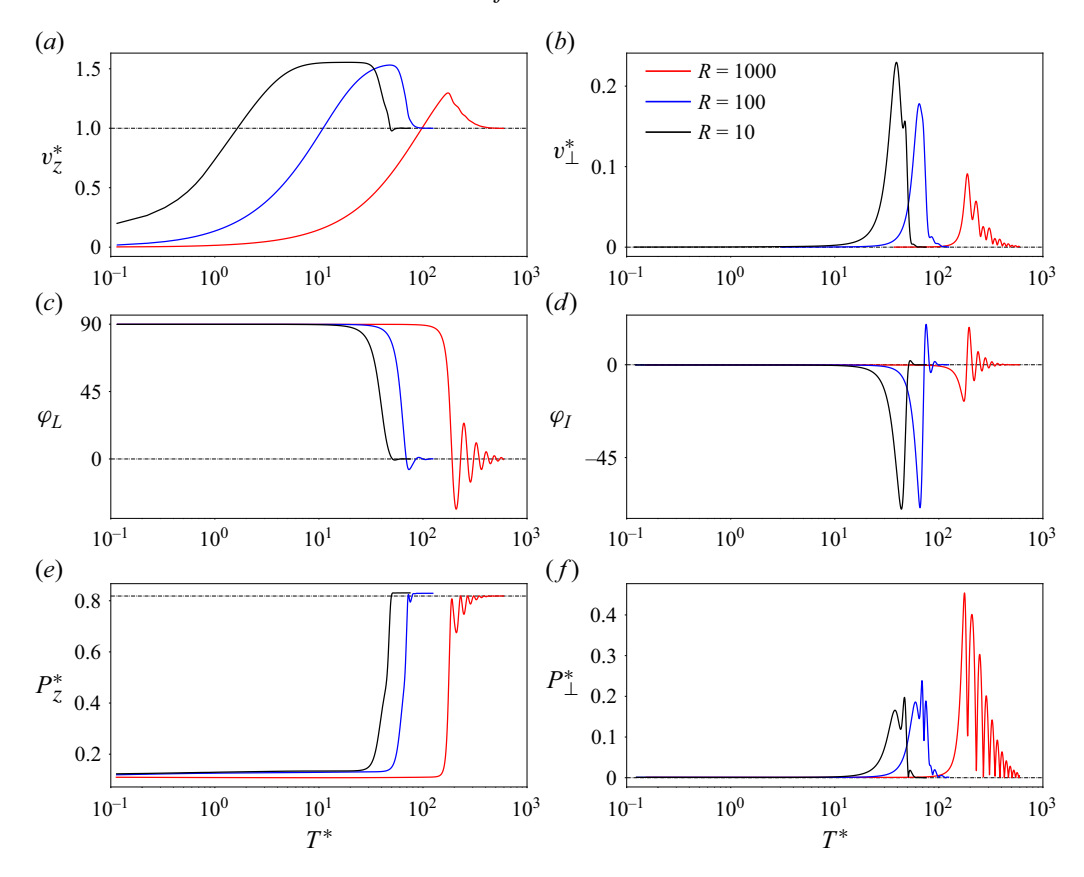


Figure 6. Various EL = FL = 0.3 particle quantities at different density ratios R = 1000, 100 and 10: (a) normalised vertical velocity $v_z^* = v_z/v_T$, where v_T is the terminal velocity; (b) normalised magnitude of lateral velocity $v_\perp^* = (v_x^2 + v_y^2)^{0.5}/v_T$; (c) pitch angle φ_L (L-axis angle from horizon); (d) roll angle φ_I (I-axis angle from horizon); (e) normalised pressure component of the drag force in the vertical direction, $P_z^* = P_z/F_z$, where F_z is the vertical component of drag force; (f) normalised magnitude of pressure components of the drag force in the lateral direction, $P_\perp^* = (P_x^2 + P_y^2)^{0.5}/F_z$. The normalised time T^* is calculated as tv_T/D_{eq} . The transient dynamics of R = 10 and 100 particles show a rapid damping of angular oscillations and a significantly lower P_\perp^* compared to the R = 1000 particle.

significant difference can be seen in figure 6(e,f) with regard to the contribution of the pressure component of the drag force. In particular, a large lateral pressure component of the drag force P_{\perp}^* development is recorded for R=1000, which also correlates with the lateral drifts during each twist and turn. These simulations support the conclusion that the ratio of particle to liquid density R is a key parameter governing the settling pattern, lateral dispersion, and evolution of velocity and hydrodynamic forces for free-falling, non-spherical particles, even at low Reynolds numbers considered in this study.

3.4. Detailed settling dynamics at R = 1000

We now turn our attention to the particle with EL = FL = 0.3 and R = 1000 to understand the fundamental physical processes behind twists and turns (figure 7a,b) in the particle trajectories. This particle serves as a representative case for all other shapes, as it exhibits a combination of all the dynamics observed in other cases studied here, allowing us to study settling dynamics in more detail without analysing each case individually. Figure 7(a) shows that the particle follows a non-planar, nonlinear 3-D trajectory characterised by

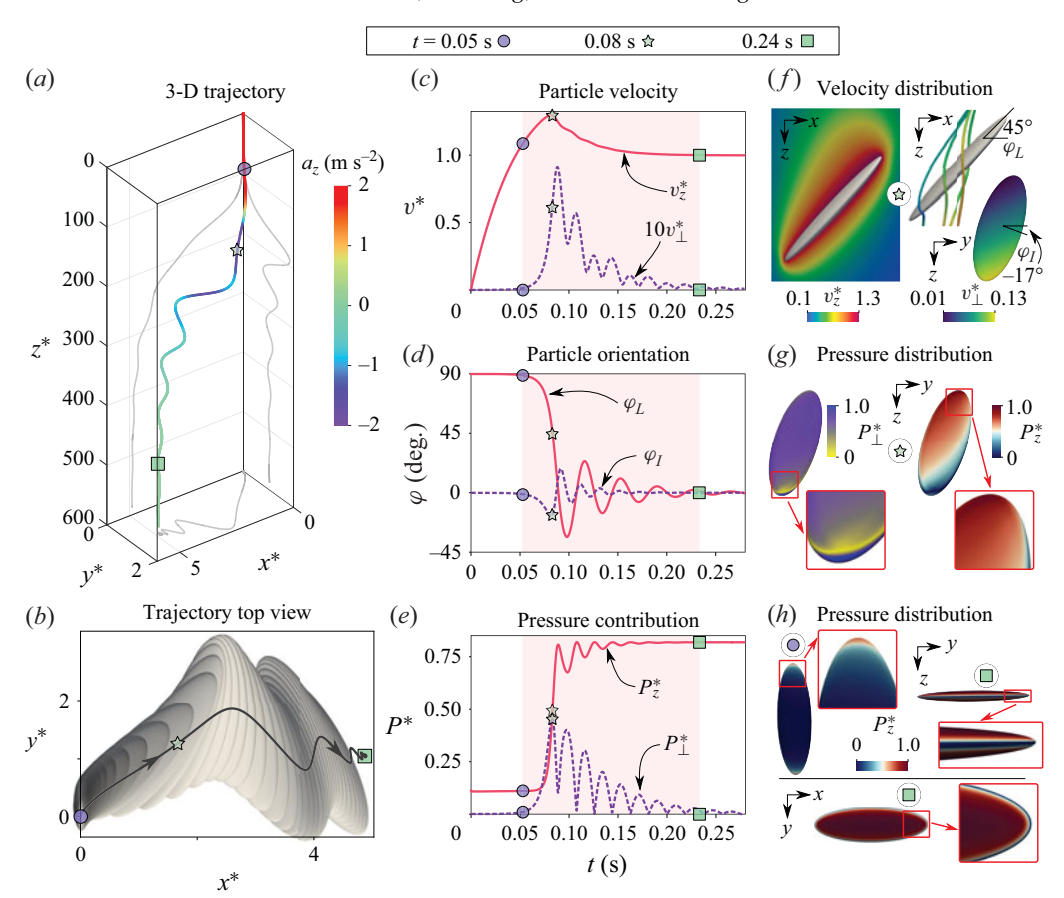


Figure 7. Settling dynamics of EL = FL = 0.3 particle at density ratio R = 1000 in air. (a) The 3-D particle trajectory (coloured by the instantaneous acceleration a_z) and its two-dimensional projections (grey) at $Re_p = 3$. Different transient phases are marked by: circle – start of angular motion, star – a pitch angle φ_L (L-axis angle from horizon) of 45° , and square – onset of terminal state. (b) Top view of the particle trajectory together with the superimposed particle images. Time t evolutions of: (c) particle velocity normalised by terminal velocity $\mathbf{v}^* = \mathbf{v}/v_T$ (v_z^* is the vertical component, and v_\perp^* is the magnitude of the lateral components); (d) particle orientation (φ_L is the pitch angle, and φ_I is the roll angle – I-axis angle from horizon); and (e) the particle's pressure components of the drag force $P^* = P/F_z$ normalised by the vertical component of the drag force F_z (P_z^* and P_\perp^* are respectively the vertical component and the magnitude of the lateral components). At $\varphi_L = 45^\circ$ ($\varphi_I = -17^\circ$): (f) the velocity distribution and streamlines of airflow around the particle (coloured based on v_z^*), and the surface distribution of v_z^* ; and (g) the surface distributions of P_z^* and P_z^* . (h) The surface distribution of P_z^* at $\varphi_L = 0^\circ$ and 90° .

alternating phases of acceleration and deceleration. As depicted in figure 7(b), the particle rotates about all three axes, with pronounced pitch (i.e. L-axis angle from horizon) and yaw (i.e. S-axis angle from horizon) motions clearly visible in the top-view projection. The transient motion of the R = 1000 particle occurs in three phases (figure 7): (i) an initial acceleration phase – the particle accelerates from zero initial velocity without changing the initial orientation; (ii) a damped angular oscillation phase – the particle undergoes angular motion that results in lateral drift; and (iii) a terminal state – the particle stabilises to a terminal orientation with which it reaches the terminal velocity.

During the initial phase – until 0.05 s of time in the transient motion, which is marked with the purple circles in figure 7 – the particle retains its orientation while accelerating,

resulting in no lateral drift or lateral velocity v_{\perp}^* (figure 7c). Its pitch φ_L and roll φ_I angles remain at their initial values 90° and 0°, respectively (figure 7d). At this stage, the vertical P_z^* and lateral P_{\perp}^* pressure components of the drag force are minimal, indicating that skin friction dominates (figure 7e,h).

Beyond 0.05 s of time (purple circles in figure 7), the particle enters an angular oscillation phase, marked by rapid changes in pitch and roll angles (figure 7d), and a sharp rise in lateral velocity v_{\perp}^* – up to 14% of the terminal vertical speed (figure 7c). The proportion of pressure components of the drag force P^* also increases significantly (figure 7e). As the pitch angle passes $\varphi_L = 45^{\circ}$, the vertical velocity v_z^* overshoots by approximately 30%. At this orientation (grey stars in figure 7), the lateral surface velocity becomes notably uneven (figure 7f), with a lateral pressure component of the drag force contribution P_{\perp}^* reaching ~50% of its vertical counterpart P_z^* (figure 7e). This ensuing asymmetric distribution of pressure components of the drag force (figure 7g) induces torques in both lateral and vertical directions, causing pronounced twisting and turning as the particle settles towards its terminal state in a nonlinear manner.

The particle's orientation oscillates with two distinct frequencies: 26.9 Hz for pitch φ_L , and 51.8 Hz for roll φ_I , decaying exponentially at rates 21.2 Hz and 40.2 Hz, respectively (figure 7d). Oscillations in v_{\perp}^* , P_z^* and P_{\perp}^* match the pitch frequency, while the roll angle has minimal effect. Here, P_{\perp}^* is in phase with φ_L , whereas v_{\perp}^* and P_z^* lag by 90°. By 0.24 s of time in the transient motion (green squares), the particle settles into its terminal orientation – maximising cross-sectional area against gravity – and all parameters remain constant: $v_z^* = 1.0$ and $v_{\perp}^* = 0.0$, $\varphi_L = \varphi_I = 0^\circ$, and $P_z^* = 0.82$ and $P_{\perp}^* = 0.0$. Comparisons across density ratios (figures 5c and 6) show that at $Re_p \approx 1$, these complex trajectories and recurrent angular oscillations only arise at high R, despite the absence of flow separation or recirculation as shown in figure 7(f).

3.5. Angular dynamics at R = 1000

Figures 8 and 9 show the evolutions of the pitch, roll and yaw angle deviations from the horizon as functions of time for four particle shapes corresponding to those presented in figure 5, but only from R = 1000 simulations. These angles are defined as $\varphi_{\Gamma} = \sin^{-1}(n_z)$, where $\mathbf{n} = (n_x, n_y, n_z)$ is the unit vector along axis $\Gamma \in \{L, I, S\}$. For all these particles, the initial orientation is given by $\varphi_L = 90^\circ$ and $\varphi_I = \varphi_S = 0^\circ$, while the terminal orientation is $\varphi_S = 90^\circ$ and $\varphi_L = \varphi_I = 0^\circ$. As a result, φ_L and φ_S should definitely change their initial values, while for φ_I , it is not necessary to change value to reach the terminal orientation.

The most straightforward cases are the spheroids shown in figures 8(a) and 8(d), which exhibit a damped oscillatory transient as φ_L (or φ_S) progresses from 90° (or 0°) in perfect synchrony towards 0° (or 90°), while φ_I remains unchanged. For the triaxial ellipsoid with EL = FL = 0.3, shown in figure 8(c), all three angles show damped oscillations towards the terminal state, albeit each in a very different manner. While the behaviour of φ_L is similar to that of the spheroids, φ_S is not in sync with it. Furthermore, φ_S approaches its terminal value in a peculiar way, bouncing back below 90° twice before starting to oscillate around it. On the other hand, φ_I exhibits damped oscillations around 0° throughout the whole process. In contrast, the triaxial ellipsoid with EL = FL = 0.8 shown in figure 8(b) exhibits yet another type of angular dynamics. Remarkably for this shape, φ_I flips to 90° during the first half of the transient, then relaxes back to 0° during the second half, both times through damped oscillations. For this particle, φ_L changes only during the first half, while φ_S changes only during the second half.

The angular dynamics shown in figure 9, as expected, depict the same trends discussed above; however, here the magnitude of the angular velocities reveals another aspect

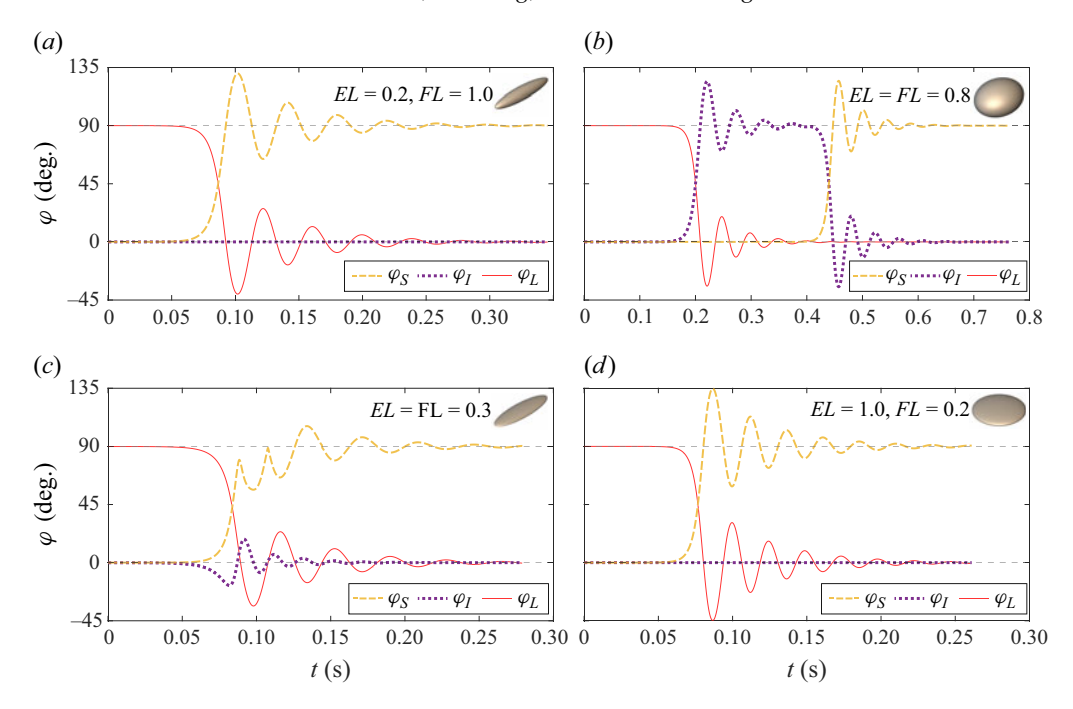


Figure 8. Evolution of pitch φ_L , roll φ_I and yaw φ_S angles at density ratio R=1000 for four ellipsoids with (a) EL=0.2, FL=1.0 (category II), (b) EL=FL=0.8 (category I), (c) EL=FL=0.3 (category III) and (d) EL=1.0, FL=0.2 (category IV) from the simulations.

of the settling dynamics. In particular, it is evident that the highest angular velocity occurs for the oblate spheroid with EL=1.0, FL=0.2, for which both $\dot{\varphi_L}$ and $\dot{\varphi_S}$ reach 227 rad s⁻¹ (figure 9d), while for the prolate spheroid they peak at approximately 140 rad s⁻¹ (figure 9a). For a triaxial ellipsoid with EL=FL=0.8, $\dot{\varphi_L}$ and $\dot{\varphi_I}$ reach 96 rad s⁻¹ in the first phase, while in the second phase, $\dot{\varphi_I}$ and $\dot{\varphi_S}$ reach a higher peak at approximately 115 rad s⁻¹ (figure 9b). Finally, for the triaxial ellipsoid with EL=FL=0.3, $\dot{\varphi_L}$, $\dot{\varphi_I}$ and $\dot{\varphi_S}$ peak at approximately 142, 106 and 151 rad s⁻¹, respectively, with $\dot{\varphi_S}$ being the first to reach its maximum.

3.6. Phase-diagrams of settling dynamics of ellipsoids at R = 1000

In this subsection, we systematically explore a broad range of ellipsoid shapes in both simulations and experiments, parametrised by elongation EL and FL (figure 10). Comprehensive datasets of key particle quantities – such as terminal velocity v_T , oscillation frequency f, decay rate of the angular oscillation μ , and other relevant quantities for each particle shape – are tabulated in tables 2–5. The particle to fluid density ratio R is 1000 for all cases shown in these tables, containing both simulation and experimental observations. Figure 10 contains the contour plots of these tabulated particle quantities in the phase space of particle elongation EL and flatness FL.

Over the examined phase space of particle shape, the terminal velocity v_T varies by a factor of 2.5 (figure 10a), having similar sensitivity to both elongation and flatness, resembling ellipsoids in the Stokes regime (Bagheri & Bonadonna 2016). This factor – the normalised terminal velocity – is inversely proportional to the ratio of the particle's surface area to that of its volume-equivalent sphere. Elongated or flattened ellipsoids fall

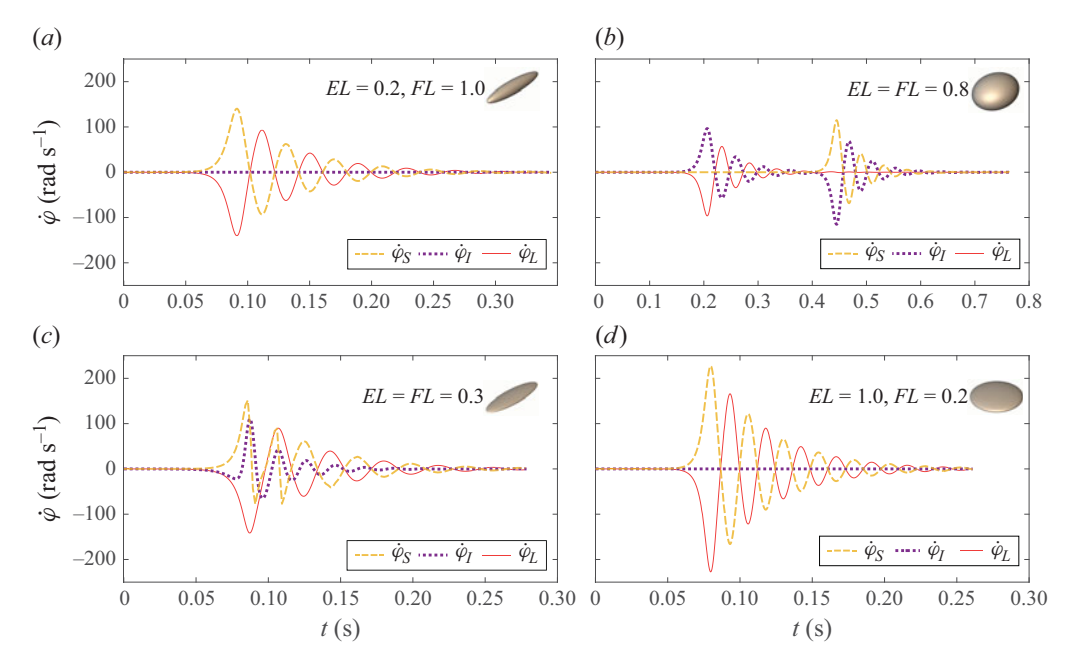


Figure 9. Evolution of the angular velocities of the pitch $\dot{\varphi}_L$, roll $\dot{\varphi}_I$ and yaw $\dot{\varphi}_S$ angles at density ratio R=1000 for four ellipsoids with (a) EL=0.2, FL=1.0 (category II), (b) EL=FL=0.8 (category I), (c) EL=FL=0.3 (category III) and (d) EL=1.0, FL=0.2 (category IV) from the simulations.

with increased surface area in the direction of gravity in the terminal state that leads to increased air resistance, thus reducing v_T compared to the volume-equivalent sphere.

In contrast, the angular oscillation frequency f peaks for flattened, non-elongated particles, showing up to a twofold increase (figure 10b). Consistent with the trends observed for pitch angular velocities in the preceding subsection, oblate shapes (category IV) exhibit the highest oscillation frequencies, peaking at approximately 40.6 Hz for the oblate spheroid with EL=1.0 and FL=0.2. Specifically, the category IV particles have median oscillation frequency 37.6 Hz and standard deviation $\sigma=1.9$ Hz. In comparison, categories II and III display moderate frequencies, with median values 29.6 Hz and 29.5 Hz, and standard deviations $\sigma=2.8$ Hz and $\sigma=4.5$ Hz, respectively. Category I, representing the near-spherical shapes, exhibits the lowest oscillation frequencies, with median 25.1 Hz and standard deviation $\sigma=6.2$ Hz, indicating greater variability among the particles in this group.

The highest exponential decay rates, denoted by μ , are observed for the oblate spheroids. However, across all ellipsoidal shapes considered, μ ranged from 18.9 Hz to 24.2 Hz with standard deviation 1.4 Hz, indicating that the decay dynamics is only weakly dependent on the particle shape. For the three experimentally and numerically measurable quantities – i.e. terminal velocity v_T , oscillation frequency f and exponential decay rate μ – we find close agreement between experiments and simulations, as shown in tables 2–5. Although the experimental set-up did not allow precise control of the initial release velocity, and almost no control of the particle orientation, this agreement shows that the transient dynamics for the considered set of shapes and Reynolds numbers is essentially independent of the initial conditions. Furthermore, the observed agreement also validates the experimental design, the data post-processing procedures, and the configuration of the numerical simulations, e.g. mesh resolution and domain size.

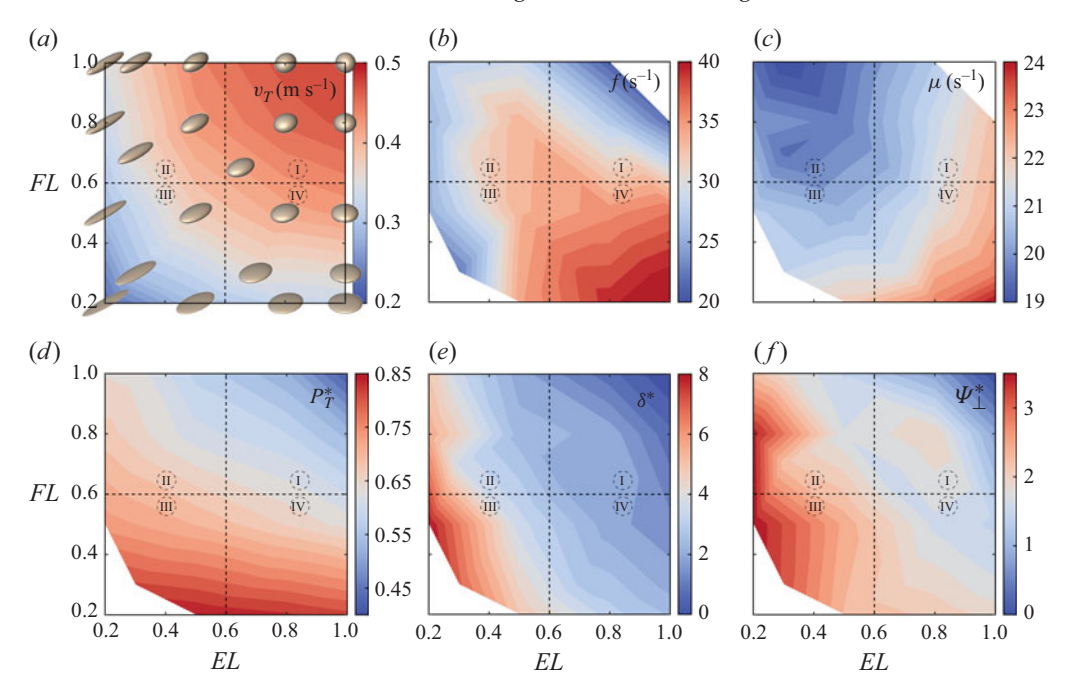


Figure 10. In the phase space of particle elongation EL and flatness FL, the distributions of (a) the terminal velocity v_T , (b) the oscillation frequency of the angular orientation f, (c) the decay rate of the oscillation amplitudes μ , (d) the terminal state contribution of pressure component of the drag force in the vertical direction P_T^* , (e) the normalised lateral drift δ^* , and (f) the normalised lateral swept volume Ψ_{\perp}^* . The scattered data are linearly interpolated using grid data in Matlab (R2023b). In the transient motion of a sphere, f and μ are not present, which are shown as white triangles in the upper right corners of (b) and (c). For ellipsoid EL = FL = 0.2, only v_T was measured. The diagrams in (a) and (b) show values from the experiments, while (c-f) are from the DNS. See table 1 for the main characteristics of the particles. Note that R = 1000 for all the particles shown in this figure. Detailed tabulated data used to produce parts of this figure are in tables 2–5.

The DNS allow us to consistently compare quantities such as lateral drift and swept volume under a fixed initial condition – zero initial velocity and minimum projection area normal to gravity – and to analyse force distributions and secondary oscillations around the intermediate axis. The terminal-state pressure component of the drag force contribution, P_T^* , expressed as the fraction of the total vertical drag, shows a strong dependence on particle flatness (figure 10d). It increases from 43% for a sphere (EL = FL = 1.0) to 82% for a highly flattened ellipsoid with EL = FL = 0.3. For comparison, the pressure component of the drag force contribution for a sphere in the Stokes regime ($Re_p \ll 1$) is approximately one-third ($P_T^* \approx 33\%$), increasing to 43% at the larger Reynolds number investigated here ($Re_p = 4.5$). This trend is expected: as Re_p increases, inertial effects become more pronounced and increasingly influence the pressure field around the particle, while the relative contribution of viscous stresses, important for frictional drag, diminishes. For all non-spherical shapes examined, P_T^* exceeds that of the sphere, indicating that the pressure component of the drag force becomes more dominant as the particle becomes more non-spherical.

To analyse transient quantities such as the swept volume and lateral drift from DNS, we consider the entire transient motion of the particles from the fixed initial condition to the terminal state. In contrast to P_T^* , lateral drift $\delta^* = \delta/D_{eq}$ depends more on elongation (figure 10e), echoing experimental trends (figure 4b) despite unavoidable initial-condition variations in experiments. The DNS reveal no drift for a sphere (EL = FL = 1.0) but up

Category no.	EL	FL	$v_T^D (\mathrm{m s^{-1}})$	$\langle v_T^E \rangle ({\rm m s^{-1}})$	$\sigma(v_T^E)~(\mathrm{ms^{-1}})$	$\#^E$
I	1.00	1.00	0.4846	0.4837	0.0024	15
I	0.80	0.80	0.4649	0.4628	0.0004	07
I	0.65	0.65	0.4349	_	_	_
I	1.00	0.80	0.4754	0.4750	0.0027	13
I	0.80	1.00	0.4826	0.4780	0.0028	15
II	0.50	1.00	0.4523	0.4436	0.0009	15
II	0.30	1.00	0.4079	_	_	_
II	0.20	1.00	0.3630	0.3519	0.0031	13
II	0.50	0.80	0.4336	0.4290	0.0036	08
II	0.20	0.80	0.3461	0.3372	0.0025	12
II	0.30	0.70	0.3766	0.3648	0.0015	10
III	0.50	0.50	0.3885	0.3845	0.0010	12
III	0.30	0.30	0.2982	0.3050	0.0050	02
III	0.20	0.20	_	0.2301	0.0022	04
III	0.50	0.20	0.3000	0.3022	0.0023	09
III	0.20	0.50	0.3037	0.3008	0.0020	11
IV	1.00	0.50	0.4306	0.4268	0.0016	13
IV	1.00	0.30	0.3831	_	_	_
IV	1.00	0.20	0.3405	0.3371	0.0018	05
IV	0.80	0.50	0.4204	0.4173	0.0013	09
IV	0.80	0.20	0.3309	0.3304	0.0007	04
IV	0.70	0.30	0.3654	0.3638	0.0019	06

Table 2. Data on particle quantities 1: v_T^D is the terminal velocity of the particle from the DNS (the magnitude of vertical velocity when the absolute magnitude of vertical acceleration $|a_z^D|$ reaches $\leq 0.01~\mathrm{m~s^{-2}}$), $\langle v_T^E \rangle$ is the terminal velocity from the experiments (the average of v_T^E from different experimental runs of each shape), and v_T^E from an experimental run is calculated by taking the average of the vertical velocities of the particle for the last 80 recorded frames when the absolute magnitude of the average vertical acceleration during these 80 frames, $|\langle a_z^E \rangle|$, reaches $\leq 0.2~\mathrm{m~s^{-2}}$. The standard deviation in the statistics for v_T^E is given as $\sigma(v_T^E)$, and the number of experimental runs used for each particle shape is denoted $\#^E$.

to $8D_{eq}$ for EL = 0.2 and FL = 0.5. We also quantify the volume swept by the particle as it reaches terminal velocity via the lateral swept volume Ψ_{\perp}^* , normalised by particle volume, which reaches 3.5 for elongated ellipsoids, and is zero for a sphere (figure 10f). Meanwhile, the normalised vertical swept volume Ψ_z^* is proportional to the terminal-state orientation of the particle, and increases from 1 (sphere) to 3.7 for the shapes investigated (table 5).

4. Discussion and concluding remarks

Using a combination of experimental observations and numerical simulations, it is demonstrated that even at particle Reynolds numbers as low as 2.1–4.5, the settling of heavy particles (i.e. R = 1000) exhibits complex angular dynamics and fully 3-D trajectories. The fact that these behaviours are consistently observed in both experiments and simulations – with excellent quantitative agreement – strongly supports their reliability, effectively ruling out the influence of experimental bias or numerical artefacts. Moreover, the results presented here clearly confirm that these dynamics arise from the large particle-to-fluid density ratio, as corroborated by additional simulations conducted at R = 10 and R = 100.

Various aspects of the settling behaviour, including particle trajectories, angular velocities, oscillation frequencies, forces acting on the particle, and flow structures, are

Category no.	EL	FL	f_L^D (Hz)	f_I^D (Hz)	$\langle f_L^E \rangle$ (Hz)	$\sigma(f_L^E)$ (Hz)	$\#^E$
I	1.00	1.00	_		_	_	
I	0.80	0.80	28.17	_	27.93	00.95	02
I	0.65	0.65	34.26	_	_	_	_
I	1.00	0.80	22.10	_	22.41	01.75	04
I	0.80	1.00	20.93		21.45	01.65	09
II	0.50	1.00	29.95	_	29.25	02.50	09
II	0.30	1.00	29.44	_	_	_	_
II	0.20	1.00	25.57	_	27.85	02.03	15
II	0.50	0.80	32.43	_	33.86	03.12	16
II	0.20	0.80	25.09	28.57	26.35	01.04	08
II	0.30	0.70	29.67	34.93	30.58	01.38	15
III	0.50	0.50	33.51	39.61	33.96	00.48	03
III	0.30	0.30	26.88	51.84	23.00	00.02	02
III	0.20	0.20	_	_	_	_	_
III	0.50	0.20	32.06	49.58	34.88	05.49	07
III	0.20	0.50	23.79	_	25.74	02.12	08
IV	1.00	0.50	36.03	_	37.09	01.23	10
IV	1.00	0.30	40.41	_		_	_
IV	1.00	0.20	40.57	_	42.02	00.00	01
IV	0.80	0.50	36.69	_	35.77	01.38	10
IV	0.80	0.20	38.04	_	39.71	03.10	06
IV	0.70	0.30	37.17	_	38.34	02.97	09

Table 3. Data on particle quantities 2: f_L^D and f_L^D are the frequencies of the angular oscillations of the pitch angle φ_L and roll angle φ_I , respectively, from the DNS, $\langle f_L^E \rangle$ is the frequency of the angular oscillations of the pitch angle φ_L from the experiments (the average of f_L^E from different experimental runs of each shape), and f_L^E from an experimental run is calculated by fitting an exponentially decaying model $\exp{(-\mu_L^E \times t + C)}$ that fits the peaks of the experimental φ_L with an R^2 value $\geqslant 0.8$ when the relative error between the fitted model and φ_L peaks from the experiments is $\leqslant 20$ %. Here, μ_L^E is the decay rate of the oscillation amplitudes of φ_L . The standard deviation in the statistics for f_L^E is given as $\sigma(f_L^E)$.

presented and discussed in detail for representative cases. All non-spherical particles examined at R=1000 exhibit damped oscillatory motion during the transient phase of their settling motion. However, while the trajectories remain planar for spheroidal particles, they become fully 3-D for some triaxial (non-axisymmetric) ellipsoids. This transition arises from the asymmetric distribution of hydrodynamic forces acting both vertically and in the lateral direction, which in turn influences the angular oscillations and overall trajectory. Whereas spheres exhibit no lateral drift, triaxial ellipsoids in our study are observed to drift laterally by up to ten times their volume-equivalent diameter. This leads to a substantial increase in the swept volume, which is directly linked to collision and encounter rates (Arguedas-Leiva *et al.* 2022), thereby enhancing the potential for particle aggregation in particle-laden flows.

Furthermore, the systematic investigation of ellipsoids of various shapes presented in this study allows us to comprehensively demonstrate the complex and nuanced dependence of settling behaviour on particle shape. The relationship between particle shape and key dynamic quantities is shown to be rich and highly non-trivial. For instance, while the settling velocity is similarly sensitive to both elongation and flatness along the symmetry axis (i.e. EL = FL), the oscillation frequency exhibits a different pattern, displaying symmetry about the orthogonal diagonal, and larger for the flattened particles. The contribution of pressure components of the drag force is also found to be strongly governed

Category no.	EL	FL	μ_L^D (Hz)	μ_I^D (Hz)	$\langle \mu_L^E \rangle$ (Hz)	$\sigma(\mu_L^E)$ (Hz)	$\#^E$
I	1.00	1.00		_	_	_	_
I	0.80	0.80	21.30	_	19.44	00.05	02
I	0.65	0.65	20.42	_	_	_	_
I	1.00	0.80	22.31	_	22.43	03.76	04
I	0.80	1.00	20.94		21.76	03.56	09
II	0.50	1.00	19.61	_	18.27	02.37	09
II	0.30	1.00	18.92	_	_	_	_
II	0.20	1.00	19.65	_	21.21	02.18	15
II	0.50	0.80	19.77	_	21.26	01.68	16
II	0.20	0.80	20.18	39.17	19.85	02.07	08
II	0.30	0.70	19.59	34.74	21.96	02.67	15
III	0.50	0.50	20.51	31.67	21.38	00.42	03
III	0.30	0.30	21.17	40.22	19.92	01.69	02
III	0.20	0.20	_	_	_	_	_
III	0.50	0.20	22.05	32.76	25.03	01.78	07
III	0.20	0.50	20.99		21.41	01.91	08
IV	1.00	0.50	22.59		23.11	02.39	10
IV	1.00	0.30	23.07	_	_	_	_
IV	1.00	0.20	24.18	_	23.87	00.00	01
IV	0.80	0.50	21.63	_	23.51	03.19	10
IV	0.80	0.20	23.06	_	20.22	05.08	06
IV	0.70	0.30	21.58	_	21.84	03.61	09

Table 4. Data on particle quantities 3: μ_L^D and μ_I^D are the decay rates of the oscillation amplitudes of the pitch angle φ_L and roll angle φ_I , respectively, from the DNS, $\langle \mu_L^E \rangle$ is the decay rate of the oscillation amplitudes of the pitch angle φ_L from the experiments (the average of μ_L^E from different experimental runs of each shape), and μ_L^E from an experimental run is calculated by fitting an exponentially decaying model exp $(-\mu_L^E \times t + C)$ that fits the peaks of the experimental φ_L with an R^2 value $\geqslant 0.8$ when the relative error between the fitted model and φ_L peaks from the experiments is $\leqslant 20$ %. The standard deviation in the statistics for μ_L^E is given as $\sigma(\mu_L^E)$.

by flatness. In contrast, lateral drift and the resulting swept volume are primarily influenced by particle elongation. These findings highlight that the dynamics of heavy particles settling in air and their dependence on particle shape are remarkably complex, even in the relatively low Reynolds number regime considered here, where instabilities such as wakes and recirculation zones are absent.

Revisiting figure 1, our findings suggest that the dynamics observed in this study may have significant implications for the behaviour of naturally occurring particles. In nature, far more pronounced non-sphericity (Magono & Lee 1966; Um et al. 2015; Bagheri & Bonadonna 2016; Zhang et al. 2020b; Xiao et al. 2023; Tatsii et al. 2023) suggests even stronger lateral transport, particle encounters and aggregation, which ultimately affect atmospheric residence times. For example, typical ice crystals (Auer & Veal 1970) and microplastics (Zhang et al. 2020b; Tatsii et al. 2023) can have much smaller flatness or elongation than studied here, potentially leading to even larger swept volumes and lateral drift. This mechanism may help to explain large-scale transport and loose-aggregate formation in volcanic ash and snowflakes. Turbulence further complicates settling orientation (Pumir & Wilkinson 2016; Voth & Soldati 2017; Mathai, Lohse & Sun 2020; Tinklenberg, Guala & Coletti 2025) and can amplify or weaken settling instabilities, making the dynamics of atmospheric particles even more complex. The full implications of the findings presented here, and the extent to which they may influence

T. Bhowmick,	Y.	Wang.	I.	Latt and	G.	Bagheri
1. Ditowillion,		110112,	,.	Dan ana	\circ .	Dugner

Category no.	EL	FL	$P_T^*\left(\%\right)$	δ (mm)	Ψ_z^*	Ψ_{\perp}^{*}
I	1.00	1.00	42.66	0.000	1.000	0.000
I	0.80	0.80	59.09	0.307	1.250	2.048
I	0.65	0.65	64.54	0.298	1.539	1.629
I	1.00	0.80	54.27	0.124	1.160	0.929
I	0.80	1.00	53.18	0.129	1.074	0.912
II	0.50	1.00	58.42	0.296	1.258	1.528
II	0.30	1.00	64.34	0.512	1.494	1.969
II	0.20	1.00	64.94	0.714	1.711	2.300
II	0.50	0.80	61.85	0.354	1.462	1.738
II	0.20	0.80	68.12	0.809	1.980	3.558
II	0.30	0.70	68.30	0.531	1.904	2.293
III	0.50	0.50	71.14	0.516	2.000	2.524
III	0.30	0.30	81.85	0.996	3.329	3.232
III	0.20	0.20	_	_	_	_
III	0.50	0.20	85.58	0.708	3.684	2.396
III	0.20	0.50	74.40	1.143	2.714	3.616
IV	1.00	0.50	64.28	0.235	1.588	1.510
IV	1.00	0.30	76.25	0.302	2.231	1.750
IV	1.00	0.20	82.26	0.374	2.924	2.003
IV	0.80	0.50	66.95	0.292	1.710	1.674
IV	0.80	0.20	83.91	0.458	3.150	2.180
IV	0.70	0.30	78.83	0.425	2.524	2.063

Table 5. Data on particle quantities 4: P_T^* is the contribution of the pressure component of the drag force to the vertical component of the drag force in the terminal state, obtained from the DNS, δ is the integral of the lateral displacements (the lateral drift, obtained from the DNS), Ψ_z^* is the vertical swept volume also obtained from the DNS, normalised by the swept volume of the volume-equivalent sphere, and Ψ_\perp^* is the lateral swept volume obtained from the DNS, normalised by the particle volume.

the dynamics of solid atmospheric particles, remain to be explored under real-world conditions, where atmospheric turbulence and the naturally occurring diversity of particle shapes are expected to play a significant role.

Supplementary movie. Supplementary movie is available at https://doi.org/10.1017/jfm.2025.10674.

Acknowledgements. This work was supported by the Max Planck Society. Scientific activities were carried out at the Max Planck Institute for Dynamics and Self-Organization (MPI-DS). Computational resources from the Max Planck Computing and Data Facility and MPI-DS are gratefully acknowledged.

Funding. T.B. was funded by the German Research Foundation (DFG) Walter Benjamin Position (project no. 463393443).

Declaration of interests. The authors report no conflict of interest.

Author contributions. Conceptualisation and research design: T.B., Y.W. and G.B. Experiments: T.B. Post-processing of the experimental data: T.B., Y.W. and G.B. Simulations: T.B. Post-processing of the simulation data: T.B. and Y.W. Analysis of the results: T.B., Y.W. and G.B. Development of simulation software: T.B., Y.W. and J.L. Visualisation: T.B., Y.W. and G.B. Interpretation of results: T.B., Y.W. and G.B. Writing – original draft: T.B., Y.W., J.L. and G.B. Writing – review and editing: T.B., Y.W., J.L. and G.B.

REFERENCES

ALLEN, S., ALLEN, D., PHOENIX, V.R., JIMÉNEZ, D., SIMONNEAU, A., BINET, S. & GALOP, D. 2019 Atmospheric transport and deposition of microplastics in a remote mountain catchment. *Nature Geosci.* 12, 339–344.

- ARGUEDAS-LEIVA, J.-A., SŁOMKA, J., LALESCU, C.C., STOCKER, R. & WILCZEK, M. 2022 Elongation enhances encounter rates between phytoplankton in turbulence. *Proc. Natl Acad. Sci. USA* 119 (32), e2203191119.
- AUER, A.H. & VEAL, D.L. 1970 The dimension of ice crystals in natural clouds. J. Atmos. Sci. 27 (6), 919–926.
- AUGUSTE, F., MAGNAUDET, J. & FABRE, D. 2013 Falling styles of disks. J. Fluid Mech. 719, 388-405.
- BAGHERI, G. & BONADONNA, C. 2016 On the drag of freely falling non-spherical particles. *Powder Technol.* **301**, 526–544.
- BAKER, L.J. & COLETTI, F. 2022 Experimental investigation of inertial fibres and disks in a turbulent boundary layer. *J. Fluid Mech.* **943**, A27.
- BARAN, A.J. 2012 From the single-scattering properties of ice crystals to climate prediction: a way forward. *Atmos. Res.* 112, 45–69.
- BELMONTE, A., EISENBERG, H. & MOSES, E. 1998 From flutter to tumble: inertial drag and Froude similarity in falling paper. *Phys. Rev. Lett.* **81** (2), 345.
- BHATNAGAR, P.L., GROSS, E.P. & KROOK, M. 1954 A model for collision processes in gases. I. Small amplitude processes in charged and neutral one-component systems. *Phys. Rev.* **94** (3), 511–525.
- BHOWMICK, T., LATT, J., WANG, Y. & BAGHERI, G. 2025a Palabos Turret: a particle-resolved numerical framework for settling dynamics of arbitrary-shaped particles. *Comput. Fluids* **299**, 106696.
- BHOWMICK, T., LATT, J., WANG, Y. & BAGHERI, G. 2025b Software Palabos Turret: a particle-resolved numerical framework for settling dynamics of arbitrary-shaped particles. Zenodo. https://doi.org/10.5281/zenodo.14928845
- BHOWMICK, T., SEESING, J., GUSTAVSSON, K., GUETTLER, J., WANG, Y., PUMIR, A., MEHLIG, B. & BAGHERI, G. 2024 Inertia induces strong orientation fluctuations of nonspherical atmospheric particles. *Phys. Rev. Lett.* **132** (3), 034101.
- BODÍ, M.B., MARTIN, D.A., BALFOUR, V.N., SANTÍN, C., DOERR, S.H., PEREIRA, P., CERDÀ, A. & MATAIX-SOLERA, J. 2014 Wildland fire ash: production, composition and eco-hydro-geomorphic effects. *Earth-Sci. Rev.* 130, 103–127.
- Brahney, J., Hallerud, M., Heim, E., Hahnenberger, M. & Sukumaran, S. 2020 Plastic rain in protected areas of the United States. *Science* **368** (6496), 1257–1260.
- CABRERA, F., SHEIKH, M.Z., MEHLIG, B., PLIHON, N., BOURGOIN, M., PUMIR, A. & NASO, A. 2022 Experimental validation of fluid inertia models for a cylinder settling in a quiescent flow. *Phys. Rev. Fluids* 7, 024301.
- VAN DER, DOES, M., KNIPPERTZ, P., ZSCHENDERLEIN, P., HARRISON, R.G. & STUUT, J.-B.W. 2018 The mysterious long-range transport of giant mineral dust particles. *Sci. Adv.* 4 (12), eaau2768.
- ERN, P., RISSO, F., FABRE, D. & MAGNAUDET, J. 2012 Wake-induced oscillatory paths of bodies freely rising or falling in fluids. *Annu. Rev. Fluid Mech.* 44 (1), 97–121.
- ESTEBAN, L.B., SHRIMPTON, J.S. & GANAPATHISUBRAMANI, B. 2020 Disks settling in turbulence. *J. Fluid Mech.* 883, A58.
- FIELD, S., KLAUS, M., MOORE, M.G. & NORI, F. 1997 Chaotic dynamics of falling disks. *Nature* 388, 252–254.
- GIURGIU, V., CARIDI, G.C.A., DE PAOLI, M. & SOLDATI, A. 2024 Full rotational dynamics of plastic microfibers in turbulence. *Phys. Rev. Lett.* 133, 054101.
- GUSTAVSSON, K., SHEIKH, M.Z., LOPEZ, D., NASO, A., PUMIR, A. & MEHLIG, B. 2019 Effect of fluid inertia on the orientation of a small prolate spheroid settling in turbulence. *New J. Phys.* 21, 083008.
- HAPPEL, J. & BRENNER, H. 1983 Low Reynolds Number Hydrodynamics. Martinus Nijhoff Publishers.
- HORWELL, C.J. & BAXTER, P.J. 2006 The respiratory health hazards of volcanic ash: a review for volcanic risk mitigation. Bull. Volcanol. 69, 1–24.
- VAN HOUT, R. & KATZ, J. 2004 A method for measuring the density of irregularly shaped biological aerosols such as pollens. *J. Aerosol Sci.* **35**, 1369–1384.
- JAYAWEERA, K.O.L.F. & COTTIS, R.E. 1969 Fall velocities of plate-like and columnar ice crystals. Q. J. R. Meteorol. Soc. 95 (406), 703–709.
- KAJIKAWA, M. 1972 Measurement of falling velocity of individual snow crystals. *J. Met. Soc. Japan* **508**, 577–583.
- KAJIKAWA, M. 1992 Observations of the falling motion of plate-like snow crystals. Part I: The free-fall patterns and velocity. *J. Met. Soc. Japan II* 70 (1), 1–9.
- KHAYAT, R.E. & COX, R.G. 1989 Inertia effects on the motion of long slender bodies. *J. Fluid Mech.* **209**, 435–462.
- LATT, J. et al. 2021 Palabos: parallel lattice Boltzmann solver. Comput. Maths Applics. 81, 334–350.
- LIU, Y., CAMPBELL, J.H., STEIN, O., JIANG, L., HUND, J. & LU, Y. 2018 Deformation behavior of foam laser targets fabricated by two-photon polymerization. *Nanomaterials* 8 (7), 498.

- LOPEZ, D. & GUAZZELLI, E. 2017 Inertial effects on fibers settling in a vortical flow. *Phys. Rev. Fluids* 2, 024306.
- MAGONO, C. & LEE, C.W. 1966 Meteorological classification of natural snow crystals. *Journal of the Faculty of Science, Hokkaido University. Series 7, Geophysics.* **2** (4), 321–335.
- MAHOWALD, N., ALBANI, S., KOK, J.F., ENGELSTAEDER, S., SCANZA, R., WARD, D.S. & FLANNER, M.G. 2014 The size distribution of desert dust aerosols and its impact on the Earth system. *Aeolian Res.* 15, 53–71.
- MANISALIDIS, I., STAVROPOULOU, E., STAVROPOULOS, A. & BEZIRTZOGLOU, E. 2020 Environmental and health impacts of air pollution: a review. *Front. Public Health* 8. https://doi.org/10.3389/fpubh.2020.00014
- MATHAI, V., LOHSE, D. & SUN, C. 2020 Bubbly and buoyant particle-laden turbulent flows. *Annu. Rev. Condens. Matt. Phys.* 11 (2020), 529–559.
- MATUS, A.V. & L'ECUYER, T.S. 2017 The role of cloud phase in Earth's radiation budget. J. Geophys. Res. Atmos. 122 (5), 2559–2578.
- MERRISON, J.P. 2012 Sand transport, erosion and granular electrification. Aeolian Res. 4, 1-16.
- NORRIS, J.R., ALLEN, R.J., EVAN, A.T., ZELINKA, M.D., O'DELL, C.W. & KLEIN, S.A. 2016 Evidence for climate change in the satellite cloud record. *Nature* **536** (7614), 72–75.
- OTA, K., SUZUKI, K. & INAMURO, T. 2012 Lift generation by a two-dimensional symmetric flapping wing: immersed boundary–lattice Boltzmann simulations. *Fluid Dyn. Res.* 44, 045504.
- PRUPPACHER, H.R. & KLETT, J.D. 2010 Microphysics of Clouds and Precipitation, 2nd edn. Springer.
- PUMIR, A. & WILKINSON, M. 2016 Collisional aggregation due to turbulence. *Annu. Rev. Condens. Matt. Phys.* 7, 141–170.
- RAMANATHAN, V., CESS, R.D., HARRISON, E.F., MINNIS, P., BARKSTROM, B.R., AHMAD, E. & HARTMANN, D. 1989 Cloud-radiative forcing and climate: results from the Earth Radiation Budget Experiment. Science 243 (4887), 57–63.
- REININGER, A.S.W., TATSII, D., BHOWMICK, T., BAGHERI, G. & STOHL, A. 2025 The atmospheric settling of commercially sold microplastics. *Atmos. Chem. Phys.* vol. 25, issue 18, pp. 10691–10705.
- ROSSI, E., BAGHERI, G., BECKETT, F. & BONADONNA, C. 2021 The fate of volcanic ash: premature or delayed sedimentation? *Nat. Commun.* 12, 1303.
- ROY, A., HAMATI, R.J., TIERNEY, L., KOCH, D.L. & VOTH, G.A. 2019 Inertial torques and a symmetry breaking orientational transition in the sedimentation of slender fibres. J. Fluid Mech. 875, 576–596.
- ROY, A., KRAMEL, S., MENON, U., VOTH, G.A. & KOCH, D. 2023 Orientation of finite Reynolds number anisotropic particles settling in turbulence. *J. Non-Newtonian Fluid Mech.* **318**, 105048.
- SUCCI, S. 2001 The Lattice Boltzmann Equation for Fluid Dynamics and Beyond. Oxford University Press.
- TATSII, D., BUCCI, S., BHOWMICK, T., GUETTLER, J., BAKELS, L., BAGHERI, G. & STOHL, A. 2023 Shape matters: long-range transport of microplastic fibers in the atmosphere. *Environ. Sci. Technol.* **58**, 671–682.
- TINKLENBERG, A., GUALA, M. & COLETTI, F. 2023 Thin disks falling in air. J. Fluid Mech. 962, A3.
- TINKLENBERG, A., GUALA, M. & COLETTI, F. 2025 The settling of perforated disks in quiescent and turbulent air. *J. Fluid Mech.* **1010**, A34.
- TSAI, R. 1987 A versatile camera calibration technique for high-accuracy 3D machine vision metrology using off-the-shelf TV cameras and lenses. *IEEE J. Robot. Autom.* **3** (4), 323–344.
- UM, J., McFarquhar, G.M., Hong, Y.P., Lee, S.-S., Jung, C.H., Lawson, R.P. & Mo, Q. 2015 Dimensions and aspect ratios of natural ice crystals. Atmos. Chem. Phys. 15 (7), 3933–3956.
- VOTH, G.A. & SOLDATI, A. 2017 Anisotropic particles in turbulence. *Annu. Rev. Fluid Mech.* **49** (1), 249–276. WILL, J.B., MATHAI, V., HUISMAN, S.G., LOHSE, D., SUN, C.& KRUG, D. 2021 Kinematics and dynamics of freely rising spheroids at high Reynolds numbers. *J. Fluid Mech.* **912**, A16.
- WILLMARTH, W.W., HAWK, N.E. & HARVEY, R.L. 1964 Steady and unsteady motions and wakes of freely falling disks. Phys. Fluids 7, 197–208.
- XIAO, S., CUI, Y., BRAHNEY, J., MAHOWALD, N.M. & LI, Q. 2023 Long-distance atmospheric transport of microplastic fibres influenced by their shapes. *Nat. Geosci.* 16, 863–870.
- ZHANG, Q., XU, E.G., LI, J., CHEN, Q., MA, L., ZENG, E.Y. & SHI, H. 2020a A review of microplastics in table salt, drinking water, and air: direct human exposure. *Environ. Sci. Technol.* **54** (7), 3740–3751.
- ZHANG, Y., KANG, S., ALLEN, S., ALLEN, D., GAO, T. & SILLANPÄÄ, M. 2020b Atmospheric microplastics: a review on current status and perspectives. *Earth-Sci. Rev.* 203, 103118.